Stagnation point flow of wormlike micellar solutions in a microfluidic cross-slot device: Effects of surfactant concentration and ionic environment

Simon J Haward* and Gareth H McKinley

Hatsopoulos Microfluids Laboratory, Department of Mechanical Engineering, Massachusetts Institute of Technology, Cambridge, MA 02139, USA

Submitted on 14th Dec 2011, in revised form 20th Feb 2012

*Corresponding author:
S.J. Haward
Massachusetts Institute of Technology
Department of Mechanical Engineering
77 Massachusetts Avenue
Cambridge MA 02139
Tel. +1 6172530273
Email: shaward@MIT.EDU

ABSTRACT

We employ the techniques of micro-particle image velocimetry (μ-PIV) and full-field birefringence microscopy combined with mechanical measurements of the pressure drop to perform a detailed characterization of the extensional rheology and elastic flow instabilities observed for a range of wormlike micellar solutions flowing through a microfluidic cross-slot device. As the flow rate through the device is increased, the flow first bifurcates from a steady symmetric to a steady asymmetric configuration characterized by a birefringent strand of highly aligned micellar chains oriented along the shear-free centerline of the flow field. At higher flow rates the flow becomes three-dimensional and time dependent and is characterized by aperiodic spatio-temporal fluctuations of the birefringent strand. The extensional properties and critical conditions for the onset of flow instabilities in the fluids are highly dependent on the fluid formulation (surfactant concentration and ionic strength) and the resulting changes in the linear viscoelasticity and nonlinear shear rheology of the fluids. By combining the measurements of critical conditions for the flow transitions with the viscometric material properties and the degree of shear-thinning characterizing each test fluid, it is possible to construct a stability diagram for viscoelastic flow of complex fluids in the cross-slot geometry.

PACS number(s): 83.80.Qr, 83.50.-v, 47.50.-d, 47.57.-s

I. INTRODUCTION

Micelles are self-assembled aggregates formed from amphiphilic surfactant molecules in solution [1, 2]. For certain surfactants, as the concentration is increased above the critical micellar concentration (cmc), initially spherical micelles can grow into cylindrical rods which eventually exceed their persistence length and become long and wormlike. Most surfactants are ionic and the formation of long wormlike micelles requires the presence of counterions of opposite charge to the surfactant in order to reduce the electrostatic interactions that act as a barrier to self-assembly. Such wormlike micelles are, in many ways, analogous to polymer molecules, though with one particularly notable difference; the ability to break and reform dynamically. In semi-dilute entangled solutions this provides additional stress relaxation mechanisms beyond reptation and allows the fluid's non-Newtonian properties to recover subsequent to events such as micellar fracturing that can occur for example in strong extensional flows [3-5]. When the characteristic breaking/reformation time of the micelles is fast compared with the reptation time, such fluids are found to exhibit almost ideal Maxwellian behaviour. The physical properties of most wormlike micellar systems (e.g. the contour length, persistence length, branching and entanglement length, and thus fluid viscoelasticity and characteristic reptation and breaking/reformation times) are extremely sensitive to factors including surfactant concentration, solvent ionic strength and temperature [1-4, 6]. This picture is further complicated when different types of counterion contributing to the ionic environment are considered individually. “Strongly-binding counterions” effectively neutralize the charged groups on the surfactant molecule by permanent attachment and therefore become physically incorporated, or “intercalated”, into the micelles, whereas the addition of simple salts such as NaCl to a surfactant solution merely results in “charge-screening” of the electrostatic interactions between surfactants and thus has a weaker effect [2]. Multivalent counterions may provide further differing and complicated effects on the micellar growth and morphology [7, 8].

The ability to control the micelle properties (and hence the bulk rheological properties) by careful tuning of the fluid composition results in a class of fluids whose rheological properties can be exquisitely manipulated according to specific formulation requirements, and which have thus become extremely important in wide-

ranging industrial and consumer applications [9-11]. While the effects of compositional changes on the shear rheology of wormlike micellar solutions have been investigated quite extensively [4, 7, 8, 12-14], systematic studies of such effects on the extensional rheology are few and have focussed on the effects of branching [15, 16]. Since many applications of wormlike micellar fluids (such as jetting and spraying, turbulent drag reduction and tertiary oil recovery) involve strongly extensional components in the flow field [11], the importance of such studies is evident. As an additional motivation, it may be possible to use subtle changes in the fluid formulation to control the critical conditions and nature of the elastic instabilities that are observed in high deformation rate flows of such fluids [17-23], which would make them particularly useful and attractive for exploitation in low Reynolds number mixing applications [24, 25] and for use in microfluidic control elements [26].

In a previous publication [19] we reported detailed experimental investigations of the extensional rheology and elastic instabilities of a single semi-dilute entangled wormlike micellar solution in a well-defined "benchmark" extensional flow field generated using a microfluidic cross-slot geometry. Cross-slot flow geometries are formed from two rectangular channels that bisect orthogonally and have opposing inlets and outlets. A singular point of zero flow velocity (a free stagnation point) is generated at the centre of the cross, and the combination of infinite residence time and finite velocity gradient at the stagnation point allows the accumulation of very high (effectively infinite) fluid Hencky strains and large extensional stresses. In complex fluids, if the velocity gradient (or strain rate, $\dot{\varepsilon}$) at the stagnation point exceeds the reciprocal of the characteristic relaxation time ($1/\lambda$) such that the Weissenberg number ($Wi = \dot{\varepsilon}\lambda$) exceeds unity, extensional stresses can overcome entropic elasticity resulting in a significant extension and alignment of any deformable microstructural elements such as polymers or micelles contained in the fluid [27-29]. Such stretching and orientation effects can result in significant increases in the fluid extensional viscosity [19, 30] and, when inertia is not significant, can give rise to purely elastic instabilities [18, 19, 22, 24, 31-35].

In this contribution we employ the same microfluidic cross-slot device and the same surfactant/counterion system of cetylpyridinium chloride and sodium salicilate

(CPyCl/NaSal) as used in our previous work, but we vary the CPyCl/NaSal concentration within the semi-dilute region of the compositional phase diagram. Salicilate is a strongly-binding counterion for the cetylpyridinium surfactant molecule [2]. We also examine the effect of the addition of NaCl to the fluid, which provides additional charge-screening chloride ions. This enables us to readily vary the rheological properties of the micellar fluids over three orders of magnitude in zero-shear viscosity and to investigate the resulting changes in fluid dynamical response within this prototypical extensional flow field. We use the techniques of micro-particle image velocimetry (μ-PIV) and full-field birefringence microscopy combined with measurements of the macroscopic pressure drop across the micro-machined cross-slot device to perform a comprehensive characterization of the extensional properties and sequence of flow instabilities exhibited by these complex fluids in the well-defined extensional flow field. Pronounced local birefringence is observed due to the orientation and alignment of micelles in the flow field, and can be used to assess the state of extensional stress [36, 37]. We find the extensional behaviour, as well as the steady and oscillatory shear rheology, is highly sensitive to the fluid composition and this enables us to map out a "state diagram" for this particular class of fluid. The remainder of this article is organized as follows: in Section II we describe the fluid preparation and characterization using standard rheological techniques, before briefly describing our extensional flow apparatus and experimental methods in Section III. Our results of extensional rheology and observations of elastic instabilities are presented in Section IV. Ultimately, the critical conditions for the onset of elastic instabilities in the various fluids are collated and summarized on a single dimensionless state diagram in Weissenberg-Reynolds number space and in Section V we conclude.

II. FLUID SAMPLES

The surfactant/counterion system used in this study (CPyCl:NaSal:NaCl) has been studied extensively and discussed at length by Rehage and Hoffman [4, 38] and Berret et al. [12]. The system is well known to form giant wormlike micelles of length on the order of micrometers and persistence length on the order of tens of nanometers [2], details which can be confirmed by cryo-transmission electron microscopy (cryo-TEM) [39]. The CPyCl and the NaSal samples were supplied by Alfa Aesar. Reagent

grade NaCl was obtained from Sigma Aldrich. Five test fluids were prepared with CPyCl:NaSal:NaCl concentrations of: 100:60:0 mM, 66:40:0 mM, 50:30:0 mM, 33:20:0 mM and 33:20:100 mM. To prepare the fluids, the CPyCl, NaSal and NaCl powders were weighed and added to the appropriate volume of deionised water. The mixture was stirred vigorously for three days and then left to equilibrate at room temperature in dry, unlit conditions for a further ten days before any experiments were conducted.

The storage and loss moduli, $G'(\omega)$ and $G''(\omega)$ of the test fluids were measured at 22˚C (close to the ambient laboratory temperature at which all subsequent cross-slot experiments were performed) using a TA Instruments AR-G2 stress-controlled rheometer with a stainless steel 40 mm diameter 2˚ cone-and-plate fixture. The results are presented in Fig. 1(a), and have been fitted with a single mode Maxwell model, given in Eq. (1) [1]:

$$G'(\omega) = \frac{G_0(\lambda_M\omega)^2}{1+(\lambda_M\omega)^2},\ G''(\omega) = \frac{G_0\lambda_M\omega}{1+(\lambda_M\omega)^2}. \quad (1)$$

From the fits to the data, values for the Maxwell relaxation time (λ_M) and plateau modulus (G_0) for the fluids were obtained and are provided in Table 1. Fig. 1(b) shows a comparison of normalized Cole-Cole plots of G''/G_0 versus G'/G_0 for all five test fluids. When plotted in this form, a purely Maxwellian fluid lies on semi-circle of radius 0.5, indicated by the dashed black line. We observe that the 100:60:0 mM test fluid is close to the ideal Maxwellian case, however the fit to a single mode Maxwell becomes worse with increasing dilution down to 33:20:0 mM. A single mode Maxwell-Debye relaxation process is only observed in wormlike micellar fluids in the "fast-breaking limit", that is when the characteristic breakage time is significantly faster than the reptation time [40, 41]. For the 100:60:0 mM fluid, we can use the Cole-Cole plot and the method described by Turner and Cates [42] to estimate the characteristic micellar breakage time ($\lambda_{break} \approx 1.25$ s) and reptation time ($\lambda_{rep} \approx 5$ s). Increasing the dilution of the fluid results in shorter, less entangled micelles, which have a shorter reptation time. In this limit, the two time scales are not well separated and Cates [40] argues that this results in a spectrum of relaxation times that can be described by a stretched exponential relaxation kernel. This is supported

by experimental measurements [4]. Fig. 1 shows that the addition of 100 mM NaCl to the most dilute surfactant solution (to make 33:20:100 mM CPyCl:NaSal:NaCl) results in a fluid which is again closely Maxwellian over a significant region. This indicates that the charge-screening effect of the Cl^- counterion encourages the formation of micelles long enough to significantly entangle and increase their reptation time. Additionally, surfactant-surfactant interactions mediated via the charge screening Cl^- ions may be weakened, resulting in a decreased breakage time.

In Fig. 2(a) we present the results of steady shear rheometry performed on the micellar test fluids in the form of a flow curve of the stress (σ) as a function of the shear rate ($\dot{\gamma}$). The corresponding shear viscosity (η) as a function of $\dot{\gamma}$ is presented in Fig. 2(b). For low shear rates, $\dot{\gamma} \leq 100$ s^{-1} this data was obtained using the AR-G2 cone-and-plate in the same configuration as previously described and is represented by the solid symbols. To access higher shear rates, up to $\dot{\gamma} \approx 10^4$ s^{-1}, a Rheosense m-VROC microfluidic rheometer was used [43, 44] and the corresponding data is shown by the hollow symbols. We find a good overlap between the two techniques. For the 100:60:0 mM test fluid at shear rates $\dot{\gamma} < 10^{-1}$ s^{-1}, pseudo-Newtonian behaviour with an essentially invariant viscosity, $\eta_0 \approx 95$ Pa s is observed. Above $\dot{\gamma} \approx 10^{-1}$ s^{-1} there is a pronounced stress plateau ($\sigma_{plateau} \approx 15$ Pa), which is indicative of the onset of shear-banding in the entangled micellar liquid [45-47]. The stress plateau spans three decades of shear rate, during which the shear viscosity thins with a power-law index of $n \approx 0$, i.e. $\eta \propto \dot{\gamma}^{-1}$. For $\dot{\gamma} > 500$ s^{-1} the shear stress begins to increase again with shear rate, according to $\sigma \propto \dot{\gamma}^{0.54}$. These measurements are in excellent agreement with those reported by previous authors on the same fluid [44, 46, 48]. As the fluid is diluted towards a final concentration of 33:20:0 mM, the zero shear viscosity plummets by three orders of magnitude (Fig. 2(b)) and the stress plateau region (Fig. 2(a)) becomes progressively shorter and less pronounced (i.e. the fluids become less shear-thinning, as expected). Indeed, for the 33:20:0 mM test fluid, no stress plateau can be discerned, although a significantly shear-thinning plateau-like region is recovered by the addition of 100 mM NaCl. The steady shear rheology of all the test fluids is well described by the Carreau-Yasuda model [49] (shown by the solid lines in Fig. 2(a) and (b)):

$$\eta = \eta_\infty + (\eta_0 - \eta_\infty)\left[1 + (\dot{\gamma}/\dot{\gamma}^*)^a\right]^{(n-1)/a} \quad (2)$$

where η_∞ is the infinite-shear-rate viscosity, η_0 is the zero-shear-rate viscosity, $\dot{\gamma}^*$ is the characteristic shear rate for the onset of shear-thinning, n is the "power-law exponent" and a is a dimensionless fitting parameter that influences the sharpness of the transition from constant shear viscosity to the power-law region. The values of these parameters determined for all the test fluids are provided in Table 1. We note that this generalized Newtonian fluid (GNF) model accurately describes the shear-thinning behaviour, but does not account for viscoelasticity, therefore its applicability is restricted. However, it has been shown that this simple model can be used to predict fully developed velocity profiles, for conditions where viscoelastic memory effects are not dominant [19]. Consistency between the two models used to fit the steady and oscillatory shear data is demonstrated by the fact that λ_M is of order $1/\dot{\gamma}^*$ for all of the test fluids and that (apart from for the 33:20:0 mM fluid, for which the oscillatory shear data is not very well fitted by the Maxwell model) $G_0\lambda_M \approx \eta_0$.

In addition to steady and oscillatory shear measurements, we also characterized the wormlike micellar solutions in a uniaxial extensional flow using a capillary breakup extensional rheometer, or CaBER device [50, 51]. This was possible for all but the most dilute (33:20:0 mM) and lowest viscosity fluid sample, which could not be made to sustain a filament for sufficient time for meaningful measurements to be obtained. The CaBER device uses measurements of capillary thinning and breakup to provide a measure of the extensional rheology of complex fluids. The test samples consist of an initially cylindrical volume of fluid ($V \approx 0.03$ mL), which forms a liquid bridge between circular parallel plates of diameter D_0 = 6 mm and initial separation $L_0 = 1$ mm (initial aspect ratio $\Lambda_0 = L_0/D_0 =$ 0.167). To minimize gravitational sagging and obtain an approximately cylindrical liquid bridge, the initial separation of the plates is chosen to be less than the capillary length $l_{cap} = \sqrt{\sigma/\rho g} \approx 1.7$ mm, where $\sigma \approx 30$ mN m^{-1} is the surface tension, $\rho \approx$ 1.0 g cm^{-3} is the fluid density, and $g = 9.81$ m s^{-2} is the acceleration due to gravity [52]. At an initial time $t_0 < 0$, the top endplate was displaced upwards following an exponential profile $L(t) = L_0 e^{\dot{\varepsilon}(t-t_0)}$ to achieve a final plate separation of L_f = 8 mm at time t = 0 s (final aspect ratio

$\Lambda_f = L_f / D_0 = 1.33$). The subsequent evolution of the liquid filament diameter ($D(t)$) was monitored at the midplane between the endplates (i.e. at $L = L_f/2$) at a sample rate of 60 Hz using a laser micrometer. Fig. 3(a) shows the evolution of the midpoint diameter $D(t)/D_0$ as a function of time obtained for each of the micellar solutions.

For a cylindrical fluid filament, we can define the instantaneous strain rate ($\dot{\varepsilon}$) and the accumulated Hencky strain (ε_H), as follows [50, 51]:

$$\dot{\varepsilon}(t) = -\frac{2}{D(t)}\frac{dD(t)}{dt} \tag{3}$$

$$\varepsilon_H(t) = \int_0^t \dot{\varepsilon}(t)dt = 2\ln\left(\frac{D_0}{D(t)}\right) \tag{4}$$

The axial force balance on the fluid column is given by:

$$\Delta\tau(t) = 3\eta_s\dot{\varepsilon}(t) + \left(\tau_{zz} - \tau_{rr}\right) = \frac{2\sigma}{D(t)} \tag{5}$$

where $2\sigma/D(t)$ is the capillary pressure driving the filament thinning process and $\Delta\tau(t)$ is the total extensional stress difference in the elongating filament.

Combining Eqs. (3) and (5), the apparent transient extensional viscosity of the stretching fluid can be calculated as follows:

$$\eta_E = \frac{\Delta\tau(t)}{\dot{\varepsilon}(t)} = -\frac{\sigma}{dD(t)/dt} \tag{6}$$

Since the flow in the CaBER instrument is essentially shear-free, we define the Trouton ratio as the ratio of the apparent extensional viscosity to the zero-shear viscosity of the solution, i.e. $Tr = \eta_E/\eta_0$. In Fig. 3(b) we report the Trouton ratios as a function of Hencky strain for all of the wormlike micellar fluids we tested. We find that all the fluids display maximum Trouton ratios of $Tr \approx$ 50, or greater, well above the Newtonian limit of Tr = 3. With dilution, there is a general increase in the maximum measured Trouton ratio, with the 33:20:100 mM fluid showing the highest increase with $Tr \approx$ 300. This is likely explained by the low fluid viscosity and high extensibility of the micelles in the 33:20:100 mM fluid, which have a reduced persistence length due to the presence of charge screening Cl^- ions. These measurements and observations are in good general agreement with previous uniaxial

extensional rheology measurements made on similar semi-dilute entangled wormlike micellar solutions [19, 53, 54].

III. EXPERIMENTAL SETUP AND PROCEDURES

A. Flow cell geometry

An optical micrograph of the microfluidic cross-slot geometry used in the study is provided in Fig. 4(a). The device was fabricated in stainless steel by the technique of wire electrical discharge machining (wire-EDM) with a channel width of w = 200 μm and depth d = 1 mm, thus providing a reasonable approximation to a 2D flow and allowing a long optical path length for the collection of birefringence signals. In all of the data presented subsequently in this paper, the inflow and outflow directions are as marked in Fig. 4(a). The elongational flow is generated along the outflow axis, and a stagnation point is formed at the centre of the cross-slot geometry (marked by the "X"). The x and y axes are as defined in Fig. 4(a) (with the z-axis normal to the plane of the page and the origin of co-ordinates at the stagnation point). Flow in the cross-slot device was driven under controlled rate conditions using a Harvard PHD Ultra syringe pump. Further details of the cross-slot construction and the flow loop are provided in our previous publication [19].

B. Extension rates and associated dimensionless groups

For a given total volume flow rate (Q) through the cross-slot device, the superficial flow velocity in the channels is $U = Q/2wd$ and the extensional strain rate ($\dot{\varepsilon}$) at the stagnation point can be approximated by:

$$\dot{\varepsilon} = \frac{2U}{w} = \frac{Q}{w^2 d}. \qquad (7)$$

This definition assumes that fluid at the stagnation point accelerates at a constant rate from zero to U over a distance $w/2$ (i.e. half a channel width), which is likely to be reasonable only if the flow is plug-like within the channels. Although this is not the case for Newtonian fluids, it has been demonstrated to be a reasonable assumption for wormlike micellar solutions at shear rates corresponding to the stress-plateau region of the flow curve (see Fig. 2(a)), when strong shear localization at the channel walls results in a plug-like velocity profile across the channels [19].

Inertial effects in the experiment are quantified by the Reynolds number, calculated using $Re = \rho U D_h / \eta(\dot{\gamma})$, where $D_h = 2wd/(w+d)$ is the hydraulic diameter, $\rho \approx$ 1000 kg m^{-3} is the fluid density, and $\eta(\dot{\gamma})$ is the shear-rate–dependent shear viscosity determined using the Carreau-Yasuda fits to the steady shear rheology measurements (see Section II). Within the cross-slot, assuming an ideal planar extensional flow, $\boldsymbol{v} = [\dot{\varepsilon}x, -\dot{\varepsilon}y, 0]$ the appropriate value of the characteristic shear rate is, $\dot{\gamma} = \sqrt{\frac{1}{2}\mathrm{II}(\dot{\boldsymbol{\gamma}})} = 2\dot{\varepsilon}$ where $\mathrm{II}(\dot{\boldsymbol{\gamma}})$ is the second invariant of the shear rate tensor $\dot{\boldsymbol{\gamma}} = \nabla\mathbf{v} + \nabla\mathbf{v}^{\mathrm{T}}$.

The Weissenberg number (*Wi*) is used to characterize the strength of elastic effects near the stagnation point. Here *Wi* is defined as the ratio of the nominal local extensional rate near the stagnation point ($\dot{\varepsilon}$) to the rate of relaxation of the fluid determined from linear viscoelastic measurements ($1/\lambda_M$), i.e. $Wi = \dot{\varepsilon}\lambda_M$. Broadly, as the imposed extension rate exceeds the rate at which the fluid microstructure can relax, the Weissenberg number exceeds unity and nonlinear elastic effects are expected to become dominant [18, 19, 29, 55, 56]. At high Weissenberg numbers Fig. 2 shows that shear-thinning in the fluid properties becomes important and hence the characteristic relaxation time of the micellar fluids will decrease. In principle, this can be incorporated by measurement of the first normal stress difference ($N_1(\dot{\gamma})$) in the fluid and the definition of a 'local relaxation time' $\lambda(\dot{\gamma}) = N_1(\dot{\gamma})/2\tau_{xy}(\dot{\gamma})$. A shear rate-dependent local Weissenberg number can then be evaluated as $Wi(\dot{\gamma}) = \lambda(\dot{\gamma})\dot{\gamma}$.

The elasticity number $El = Wi/Re$ is a dimensionless group that can be used to provide a measure of the relative importance of elastic and inertial effects in the flow field. It is a useful number for differentiating between different dynamical regimes that can be observed in microfluidic flows through complex geometries [57-61]. *El* is a quantity that represents the trajectory of a set of experiments with a given viscoelastic fluid through the *Wi*–*Re* operating space and is at least nominally independent of the flow kinematics since, for constant viscosity fluids, both *Wi* and *Re* depend linearly on the characteristic flow velocity, *U*. At flow rates where shear-thinning effects become important, the slope of this trajectory decreases because *Re* varies as $U/\eta(\dot{\gamma})$,

while the relaxation time can also show rate-dependent decreases. Such a definition better reflects the local ratio of elastic normal stresses and viscous shear stresses in a flow, but complicates comparison with numerical models, which each predict their own functional form for the effective relaxation time $\lambda(\dot{\gamma})$. For this reason we choose to base all measures of the dimensionless flow strength on the zero-shear rate properties of the fluids determined under equilibrium conditions. Such a definition is unambiguous and facilitates comparison with computational rheological models. In Section IV.C we demonstrate how to incorporate the role of shear-thinning within the form of the Carreau-Yasuda model considered in the present work.

C. Micro-particle image velocimetry

Micro-particle image velocimetry (μ-PIV) was performed on test fluid seeded with 1.1 μm diameter fluorescent tracer particles (Nile Red, Molecular Probes, Invitrogen; Ex/Em: 520/580 nm; $c_p \approx$ 0.02 wt.%). The imaging system consisted of a 1.4 megapixel, frame-straddling CCD camera (TSI Instruments, PIV-Cam) and an inverted microscope (Nikon Eclipse TE 2000-S). A 10× 0.25 NA objective was used to focus on the mid-plane of the cross-slot flow cell. The resulting measurement depth (δz_m) over which microparticles contribute to the determination of the velocity field is $\delta z_m \approx$ 50 μm [62], or ~ 5% of the depth of the flow cell, d. The fluid was illuminated by a double-pulsed 532 nm Nd:YAG laser with pulse width δt = 5 ns. The fluorescent seed particles absorb the laser light and emit at a longer wavelength. The laser light is filtered out with a G-2A epifluorescent filter, so that only the fluorescing particles are imaged by the CCD array. Images were captured in pairs with a time separation (1.2 μs < Δt < 60,000 μs) chosen to achieve an average particle displacement of approximately four pixels, optimal for subsequent PIV analysis. Image pairs were captured at a rate of approximately four pairs per second. The standard cross-correlation PIV algorithm (TSI insight software), with interrogation areas of 16 × 16 pixels and Nyquist criterion, was used to analyze each image pair. For steady flows, twenty image pairs were captured and ensemble-averaged in order to obtain full-field velocity maps in the vicinity of the stagnation point. Tecplot 10 software (TSI, Inc.) was used to generate streamlines from the velocity vector fields.

D. Birefingence microscopy

The spatial distribution of flow-induced birefringence in the vicinity of the stagnation point was measured using an ABRIO birefringence microscope system (CRi, Inc.), which has been described in detail by Shribak and Oldenbourg [63] and in a previous publication by Ober et al. [44]. Briefly, the cross-slot flow cell is placed on the imaging stage of an inverted microscope (Nikon Eclipse TE 2000-S) and the mid-plane of the flow cell is brought into focus using a 20× 0.5 NA objective. The ABRIO system passes circularly polarized monochromatic light (wavelength 546 nm) first through the sample, then through a liquid crystal compensator optic and finally onto a CCD array. To generate a single image, the CCD records five individual frames with the liquid crystal compensator configured in a specific polarization state for each frame. Data processing algorithms described by Shribak and Oldenbourg [63] combine the five individual frames into a single full-field map of retardation and orientation angle. The system can measure the retardation (R) to a nominal resolution of 0.02 nm, and has an excellent spatial resolution (projected pixel size 0.5 μm with a 20× objective lens). The relationship between retardation and birefringence is given by:

$$R = d\Delta n, \tag{8}$$

where d is the depth of the flow cell and Δn is the birefringence.

The birefringence intensity at the stagnation point of the cross-slot device can be used to determine the local extensional viscosity of the fluid (η_E) using the stress-optical rule (SOR). The SOR states that, for limited microstructural deformations, the magnitude of the birefringence (Δn) is directly proportional to the principal stress difference in the fluid ($\Delta\sigma = \sigma_{xx} - \sigma_{yy}$) [37], i.e.:

$$\Delta n = C\Delta\sigma, \tag{9}$$

where the constant of proportionality, C, is called the stress-optical coefficient. For the 100:60:0 mM CPyCl:NaSal:NaCl system at 22˚C this has been determined by Ober et al. to be C = -1.1 × 10^{-7} Pa^{-1} [44]. The apparent extensional viscosity follows from:

$$\eta_E = \frac{\Delta\sigma}{\dot{\varepsilon}} = \frac{\Delta n}{C\dot{\varepsilon}}. \tag{10}$$

E. Pressure drop measurements

A second measure of the apparent extensional viscosity, characterizing the average rheological response of all material elements flowing through the device, can be obtained from pressure measurements made across an inlet and an outlet of the cross-slot device. Two independent pressure drop measurements must be made in order to extract the extensional contribution from the viscous (dissipative) response, as is shown schematically in Fig. 4(b). First, the pressure drop is measured as a function of U for full cross-slot stagnation point flow with opposed inlets and outlets; we term this measurement ΔP_{total}. Next, one inlet and one outlet arm are shut off by closing valves in the connecting pipes and the pressure drop is again measured as a function of U for flow around a single corner of the cross-slot device. This second measurement quantifies, to first order, shearing contributions to ΔP_{total} and hence we term this measurement ΔP_{shear}. An estimate of the apparent extensional viscosity is obtained using the following equation:

$$\eta_{E,app} = \frac{\Delta P_{total} - \Delta P_{shear}}{\dot{\varepsilon}} = \frac{\Delta P_{excess}}{\dot{\varepsilon}} . \qquad (11)$$

Comparing Eqs. (10) and (11), it is clear that if the local and global measures of the extensional response are to be consistent, then the excess pressure drop, ΔP_{excess}, should be equal to the principal stress difference, $\Delta\sigma$. Moreover, a plot of Δn versus ΔP_{excess} should yield a value for the stress-optical coefficient, C, from the gradient of the resulting straight line. These relationships have recently been demonstrated to hold well for various low viscosity Boger fluids and mildly shear-thinning biological polymer solutions in a microfluidic cross-slot geometry [30] and will be tested here for the heavily shear-thinning wormlike micellar fluids.

IV. EXPERIMENTAL RESULTS

A. Observations of flow fields and optical anisotropy

Prior to testing wormlike micellar fluids in our cross-slot geometry the flow field was confirmed to be highly symmetric and stable up to Reynolds numbers of $Re \approx 20$ using a Newtonian fluid (water). We also measured velocity profiles across the inlet and outlet channels and along the channel centrelines through the stagnation point and

confirmed that these were in excellent agreement with numerical predictions for fully developed Newtonian flow. The results are presented in our previous work [19] and are not reproduced here.

In the 100:60:0 mM CPyCl:NaSal:NaCl wormlike micellar solution, various flow regimes are observed as the flow rate (or *Wi*) is increased. At very low flow rates of $Q \leq 1$ μL min^{-1} ($Wi \leq 1.2$) the flow field is steady, symmetric and Newtonian-like, as illustrated by the streamlines shown in the left-hand part of Fig. 5(a). This symmetric flow field is accompanied by a slender birefringent strand originating from the stagnation point and extending in a symmetric fashion along the outflowing stagnation point streamline (right-hand side of Fig. 5(a)). As the flow rate is increased to $Q > 1$ μL min^{-1} the flow field remains steady but develops an asymmetry. This flow asymmetry is illustrated by Fig. 5(b) for the volume flow rate $Q = 1.5$ μL min^{-1} ($Wi = 1.9$). It is clear from the streamlines in the left-hand part of Fig. 5(b) that the majority of the fluid entering via the upper inlet channel is exiting via the right-hand outlet channel, while the majority of the fluid entering via the lower inlet channel is exiting via the left-hand outlet channel. As a result, the dividing streamline along the outflow direction is skewed about the stagnation point and this results in a birefringent strand that appears to have rotated about the stagnation point, as shown in the right-hand part of Fig. 5(b). As the flow rate is increased further, the degree of flow asymmetry and the rotation of the birefringent strand increases until, for $Q > 2$ μL min^{-1} the flow realizes a state of almost complete anti-symmetry. The anti-symmetric flow state is illustrated in Fig. 5(c) for $Q = 5$ μL min^{-1}. Here effectively 100 % of fluid entering the upper channel exits via the right-hand channel, and 100 % of fluid entering the lower channel exits via the left-hand channel. The effect of this almost complete asymmetry is to eliminate the stagnation point from the centre of the cross-slot device, which results in a significant reduction in the extensional stress on the fluid and a drop in the magnitude of the birefringence observed along the dividing streamline. It should be noted that in successive experiments the flow field can become asymmetric in either direction about the stagnation point and is therefore described as a steady, symmetry-breaking, flow bifurcation. The Reynolds number at which this bifurcation occurs is extremely low ($Re \approx 10^{-6}$) so the flow transition is purely elastic in origin.

In the 100:60:0 mM fluid the regime of bifurcated flow is maintained over more than two decades in flow rate before a second, time-dependent instability develops. This is illustrated in Fig. 6 using birefringence observations made at a flow rate of $Q = 500$ μL min^{-1} (Wi = 615), where the time interval between each image in the figure is approximately 10 s. It should be noted that there is substantial time-averaging involved in acquiring these images due to the sequential 5-frame analysis algorithm employed by the ABRIO imaging system. Nevertheless, spatio-temporal fluctuations in the recorded intensity are clear. Fourier analysis of the total pressure drop measured across the cross-slot device in this time-dependent flow regime indicates that the fluctuations are aperiodic [19].

In Fig. 7 we use a montage of images of the flow birefringence in the cross-slot flow cell to illustrate the nature of the elastic instabilities observed in the four other wormlike micellar test fluids as the flow rate is increased. For the 66:40:0 mM and 50:30:0 mM test fluids (Fig. 7(a) and (b), respectively) the results are qualitatively similar to the previously discussed 100:60:0 mM fluid. Initially there is a low Wi regime of steady symmetric flow, followed by a moderate Wi regime of bifurcated flow and a high Wi regime of time-dependent flow. The primary differences are a) that a state of complete anti-symmetry is never achieved in either the 66:40:0 mM or the 50:30:0 mM fluids as is observed in the more elastic 100:60:0 mM fluid; the flow field transitions directly from being partially bifurcated to time-dependent, and b) there is some variation in the critical values of the Weissenberg numbers $Wi_c^{(1)}$ obtained for the onset of the bifurcation and $Wi_c^{(2)}$ for the onset of the time-dependent flow regimes in each fluid.

As the test fluid concentration is reduced to 33:20:0 mM CPyCl:NaSal:NaCl the fluid behaviour in the extensional flow field alters dramatically (Fig. 7(c)). The elastic instabilities are completely suppressed and the flow field remains stable and symmetric even at the highest accessible flow rates. Because of the large reduction in the solution viscosity, the Reynolds number also climbs in these experiments. However, an even more intriguing result is obtained when just 100 mM of NaCl is added to this most dilute surfactant solution. The rheology data provided in Figs. 1 to

3 illustrates that the fluid viscoelasticity and extensibility increases substantially on the addition of NaCl and, as Fig. 7(d) shows, the 33:20:100 mM micellar solution displays all the qualitative features of the most concentrated 100:60:0 mM fluid (even including the completely asymmetric flow state) at comparable values of *Wi*.

B. Birefringence, pressure drop and apparent extensional viscosity

When the flow field is in the symmetric state (i.e. for low *Wi*), the extensional rate at the stagnation point is well-defined and measurements of the birefringence at the stagnation point can be used to determine the local extensional stress difference using Eq. (9). A second, global measure of the stress can be derived from measurements of the pressure drop across the cross-slot device using Eq. (11). In Fig. 8(a) we show the maximum birefringence (Δn) measured at the stagnation point as a function of the strain rate for the five micellar test fluids. In Fig. 8(b) we show the corresponding evolution in both the total pressure drop measured across the cross-slot device (ΔP_{total}) and that measured during steady shearing flow around a single corner of the device (ΔP_{shear}). As explained in Section IIIE, if the stress difference and the excess pressure drop increase proportionally, a plot of Δn versus $\Delta P_{excess} = \Delta P_{total} - \Delta P_{shear}$ will yield a straight line that should provide a value for the stress-optical coefficient, C [30]. When we follow this procedure for the wormlike micellar solutions, we find that for most of the test fluids, we do indeed obtain a very good straight-line fit through the origin, the gradient of which we can use as a value for C (see Fig. 8(c)). The exception is for the most concentrated and strongly shear-banding 100:60:0 mM fluid, where the linear regression is poor. Shear localization in this strongly shear-banding fluid near the sharp re-entrant corners of the cross-slot results in marked changes in the local kinematics and invalidates the simple linear decomposition embodied in Eq. (11). Nonetheless, as the imposed flow strength increases, both the pressure drop required to drive the flow and the local birefringence intensity in the region of extensional deformation increase monotonically, as observed in Fig. 8(c) (hollow squares). For this 100:60:0 mM fluid we have already made independent measurements of the stress-optic coefficient in a steady simple shear flow (Ober et al. [44]). Using this value ($C = -1.1 \times 10^{-9}$ Pa^{-1}) we indicate by the broken line the expected variation in birefringence with excess pressure drop if Eqs. (10) and (11) did hold. It is clear that the results are broadly self consistent. In our earlier cross-slot study with

the 100:60:0 mM fluid [19] we also observed that there was some difference between the forms of the extensional viscosity versus strain rate curves obtained using the two methods described by Eqs. (10) and (11). As we discussed above, this difference is due to the extremely shear-thinning nature of the fluid and the fact that the excess pressure drop is a globally averaged quantity obtained from two measurements made with rather different flow configurations. Here, we see that as the micellar solution is progressively diluted and becomes less severely shear-thinning, we indeed find increasing improvement in the co-linearity of the Δn versus ΔP_{excess} data (Fig. 8(c)).

Using the gradients of these straight-line fits passing through the origin as values of the stress-optical coefficient, C, we convert the data presented in Fig. 8(a) from birefringence (or retardation, if preferred) into a principal stress difference according to Eq. (9). Subsequently, we can divide the tensile stress difference by the strain rate to obtain an estimate of the apparent extensional viscosity, $\eta_{E,app}$, of each fluid undergoing a planar elongational flow. This is plotted as a function of Wi in Fig. 8(d), with the inset showing the Trouton ratio, $Tr = \eta_{E,app} / \eta(\dot{\gamma})$, as a function of the Weissenberg number, Wi. The Trouton ratio data almost lie on a master curve which reaches a maximum value of approximately $Tr \approx 50$ at high Wi, indicating that the fluids are significantly strain hardening. This Trouton ratio is comparable with measurements made on similar fluids using capillary breakup [19, 54] and filament stretching [53] extensional rheometry techniques and is reasonably consistent with our own CaBER measurements presented in Fig. 3(b). Whereas in the CaBER measurements, we found that the addition of salt increased the extensibility of the wormlike chains and resulted in a higher maximum Trouton ratio of $Tr \approx 300$ for the 33:20:100 mM test fluid, in the cross-slot device this does not appear to be so. We note that the apparent Trouton ratio for the 33:20:100 mM fluid measured in the cross-slot device shows no sign of reaching a plateau, and may therefore be expected to increase further, however we cannot measure this continued extensional thickening due to the onset of the flow instability. This loss of flow stability illustrates one limitation of the cross-slot device as an extensional rheometer for fluids that exhibit such elastically-induced instabilities. Conversely, the cross-slot device enables access to much higher extension rates than are possible in capillary thinning devices.

C. Analysis of elastic instabilities in the wormlike micellar solutions

In Fig. 9 we show the streamlines determined experimentally in the cross-slot device for the flow of two different wormlike micellar fluids. In Fig. 9(a), for flow of the 33:20:0 mM fluid at Q = 4000 μL min^{-1}, a symmetric flow is observed; the flow through the inlet channels divides equally between the two outlet channels. The inertio-elastic flow remains stable and symmetric despite the high values of the Weissenberg and Reynolds numbers. By contrast, in Fig. 9(b) for flow of the 50:30:0 mM fluid at Q = 420 μL min^{-1}, a sharply asymmetric flow is observed and the inlet flow divides unequally between the two outlet channels. It is possible to quantify an asymmetry parameter (ΔQ) by measuring the perpendicular distances from the inlet/outlet channel walls to the points within the channels where the streamlines divide. As marked on the images in Fig. 9, we label one of these lengths w_1 and the other w_2, where $w_1 + w_2 = w = 0.2$ mm is the channel width. Assuming the flow profile across the channel is reasonably plug-like, w_1 and w_2 should be closely proportional to the volume of fluid that flows out through each of the respective exit channels. Hence, we define the asymmetry parameter as follows:

$$\Delta Q = \left| \frac{Q_1 - Q_2}{Q} \right| \approx \left| \frac{w_1 - w_2}{w} \right|, \qquad (12)$$

where Q_1 and Q_2 represent the actual volumetric flow rates contained within the sections of channel to either side of the dividing streamline.

If w_1 and w_2 are equal (i.e. the flow is symmetric, as in Fig. 9(a)) then ΔQ = 0. On the other hand, if either w_1 or w_2 is equal to zero (as is the case for completely anti-symmetric flow such as that shown in Fig. 5(c)), then $\Delta Q \rightarrow 1$. Note that besides using streamline images, the values of w_1 and w_2 can also be estimated independently by measuring the position of the birefringent strand, since the strand itself is localized along the streamline dividing the exit channels (see Fig. 5, for example).

The values of ΔQ have been calculated as a function of *Wi* for all of the micellar fluids in which a flow bifurcation was observed and the results are presented in Fig. 10. In each case, at a given Weissenberg number, repeated measurements were made and the results represent the mean values and standard deviations of the data. As

we reported in our earlier work [19], at the CPyCl:NaSal:NaCl concentration of 100:60:0 mM the flow bifurcation commences at a critical Weissenberg number of $Wi_c^{(1)} \approx 1$ and the asymmetry parameter rapidly increases to $\Delta Q = 1$ at $Wi \approx 2$. As the fluid is progressively diluted, and the fluid elasticity decreases, the value of $Wi_c^{(1)}$ increases and the maximum value of the asymmetry parameter at high Wi is reduced. The curve of ΔQ versus Wi for the weakly shear-thinning 50:30:0 mM surfactant solution is well-described by an equation of the form $\Delta Q \sim \left(Wi - Wi_c^{(1)}\right)^{0.5}$, where $Wi_c^{(1)} \approx 11.4$. However, such a relationship does not describe the evolution of the bifurcation in the other more strongly shear-thinning fluids we tested. This classical square-root dependency of the bifurcation parameter on $Wi - Wi_c^{(1)}$ has been reported previously for constant viscosity dilute polymer solutions [24, 31, 32] and also for non-shear-banding micellar solutions [18]. That we observe such a dependence with the 50:30:0 mM fluid, which does not display a marked stress plateau in the flow curve (see Fig. 2), but not with the more strongly shear-thinning fluids, supports our previously expressed conjecture that strong shear localization near the channel walls has a strong influence on the form of the bifurcation, causing it to develop very rapidly with increasing Wi due to shear localization and self-lubrication effects [19]. For the least viscoelastic 33:20:0 mM fluid, no bifurcation is observed, however the addition of 100 mM NaCl to this surfactant solution results in a large increase in the viscoelasticity and the re-establishment of a flow bifurcation very similar in form to that observed with the 100:60:0 mM fluid. We note that the two fluids that bifurcate for a critical Weissenberg number very close to unity and achieve almost complete asymmetry are the same two fluids that show the most ideally Maxwellian linear viscoelasticity (see Fig. 1) and a clear stress plateau in the flow curve, which is normally taken as a hallmark of shear-banding behaviour. That is, their relaxation is dominated by a single time λ_M which results from the fast breaking limit of the reptation and micellar breaking time scales [40, 41].

Previously we have observed that both the onset of the initial flow bifurcation and the onset of the time-dependent instability appeared to be associated with changes in the gradient of the flow curve [19]. In Fig. 11(a) we have marked the critical shear rates for

the instabilities on the flow curve for each of the current micellar test fluids, and this trend is again broadly supported by the data. The flow bifurcation occurs over the portion of the flow curve with the lowest gradient, i.e. the region of the flow curve that is broadly termed the stress plateau. Steady symmetric flow is observed only on the low shear rate, pseudo-Newtonian branch, and a three-dimensional time-dependent flow state develops on the high shear rate branch. We associate the onset of the time-dependent flow instability with the development of a highly aligned micellar state in the fluid flowing towards the intersection, resulting in tension along the curved streamlines around the corners of the cross-slot device. It is well-established that such circumstances can lead to complex spatio-temporal dynamics in viscoelastic fluid flows [64-69]. Recent experimental results in the Taylor-Couette geometry with shear-banding wormlike micellar solutions, also formulated from CPyCl/NaSal/NaCl, clearly indicate that fluctuations in the velocity field are most strongly associated with elastic instability in the high shear rate band, eventually leading to elastic turbulence at high Weissenberg numbers [70]. The results correlate well with a recently developed criterion for purely elastic instabilities in Taylor-Couette flows of shear-banding fluids [71]. The new instability criterion, which is a generalization of an existing criterion for onset of elastic instabilities [72], is formulated around considerations of the local Weissenberg number (Wi_h) within the high shear rate band and predicts three broad categories of instability: stable flow for sufficiently low Wi_h, followed by an intermediate regime which can alternate between stable and unstable states due to flow-induced changes in the boundary conditions. Finally, for sufficiently large values of Wi_h, the flow becomes time-dependent and three-dimensional in nature. These observations made in a purely shearing flow within the Taylor-Couette geometry are, perhaps surprisingly, broadly analogous to the present observations in the cross-slot device.

The slopes of the flow curves at the points where they are intersected by the stability boundaries marked on Fig. 11(a) can be quantified by defining a tangent viscosity or *consistency* $\eta_c \equiv d\sigma/d\dot{\gamma}$, as first discussed by Cox and Merz [73] in their Letter discussing interconnections between linear and nonlinear viscoelastic properties of entangled polymeric systems. Recently it has been noted that this consistency measure can, in fact, be used in conjunction with Laun's rule [74] to provide a direct estimate of

the first normal stress difference exerted by a fluid in steady shear flow [75]. Specifically, the important quantity is the difference between the conventional shear-rate-dependent viscosity $\eta(\dot{\gamma}) \equiv \sigma/\dot{\gamma}$ and the tangent viscosity η_c, which Cox and Merz argue is related to the recoverable shear in an entangled system. When scaled with the shear viscosity, the relevant dimensionless quantity appearing in the expression proposed by Sharma and McKinley [75], which measures the importance of shear-thinning in an entangled viscoelastic fluid is $S \equiv 1 - \eta_c/\eta(\dot{\gamma})$. When combined with the definitions of the viscosity and the consistency given above, this expression becomes $S = \left(1 - d\ln\sigma/d\ln\dot{\gamma}\right)$ and can be readily evaluated from the flow curve data, or from the corresponding Carreau-Yasuda model fit for each fluid. We plot this dimensionless measure of shear-thinning on the ordinate of Fig. 11(b) versus the appropriately-scaled dimensionless shear rate $\dot{\gamma}/\dot{\gamma}^*$. For a weakly viscoelastic fluid with almost constant viscosity (e.g. the diluted 33:20:0 mM solution) this quantity is close to zero. However, for a highly entangled and strongly shear-thinning fluid (such as the 100:60:0 mM fluid) this quantity can grow towards a maximum value of unity, corresponding to a shear-thinning fluid with viscosity $\eta \sim 1/\dot{\gamma}$ and a consistency approaching zero. When represented in this form, it can be seen from Fig. 11(b) that the critical conditions measured experimentally in each fluid for bifurcation to a steady asymmetric 2D flow as well as for a subsequent transition to three-dimensional time-dependent flow clearly demarcate the boundaries of a stability 'phase diagram' for cross-slot flow.

Two important points must be noted about this tentative stability map. Firstly, although the rules proposed by Cox and Merz [73], Laun [74] and Sharma and McKinley [75] were not developed with shear-banding micellar fluids in mind, it appears that this dimensionless measure still provides a consistent way of ranking the critical conditions *at onset* of elastic instability in these very strongly shear-thinning fluids. The tendency of such shear-banding fluids to localize strong deformations *after* the onset of instability is reflected in the more rapid growth of the flow asymmetry measure ΔQ with Weissenberg number, as plotted in Fig. 10. Secondly, this plot must be a projection through a more complex, three-dimensional stability diagram, because fluid elasticity, as independently measured by the ratio of elastic normal stresses acting along curved streamlines compared to viscous stresses are a necessary feature

of viscoelastically-driven instabilities in complex flows such as the cross-slot geometry. For example, sufficiently elastic dilute polymer solutions, corresponding to $S \to 0$, also show a symmetry bifurcation in cross-slot flow [24, 31, 32], therefore a critical level of shear-thinning is neither a necessary, nor sufficient condition for onset of instability and simulations with purely inelastic models such as the Carreau model would not capture the observed flow transitions. The complete stability diagram for such fluids must therefore incorporate the coupled effects of fluid inertia, fluid elasticity as well as shear-thinning in the viscometric properties. We proceed to construct such a map below.

In order to capture the competing effects of inertia and elasticity on a 2D stability map, we summarize our results on the *Wi*-*Re* "state diagram" shown in Fig. 12. The magnitude of the Weissenberg number indicates the strength of elastic effects, while the magnitude of the Reynolds number indicates the significance of inertial effects. Plotted on a log-log scale, the trajectory of each set of experiments over a range of flow rates follows an almost straight line in *Wi*-*Re* space. This is because *Re* for each fluid is inversely proportional to the viscosity, $\eta(\dot{\gamma})$, which over a wide range of shear rates broadly follows a power law in $\dot{\gamma}$ (and hence in *U*). On the other hand, the Weissenberg number for each fluid, $Wi = \lambda_M \dot{\gamma}$, always increases linearly with *U* when based on a single Maxwell time obtained from linear viscoelasticity experiments. On Fig. 12, a lower critical Weissenberg number ($Wi_c^{(1)}$) demarcates the boundary separating steady symmetric flow from bifurcated steady asymmetric flow. The value of $Wi_c^{(1)}$ increases with *Re*, indicating that this transition is suppressed by increasing inertia. Similar trends are also observed in numerical simulations of cross-slot flow bifurcations [31]. A second, higher critical Weissenberg number ($Wi_c^{(2)}$) marks the transition from steady 2D bifurcated flow to time-dependent 3D flow. As we reported previously for the 100:60:0 mM fluid [19], Fourier analysis of time-varying pressure drop measurements made for unsteady flow above $Wi_c^{(2)}$ indicate that the fluctuations in the time-dependent flow regime are aperiodic. In general the value of $Wi_c^{(2)}$ decreases slightly with *Re*, indicating that inertia also plays a role in influencing the onset of this instability.

The systematic variation of the lower and upper stability boundaries marked out in Fig. 12 are such that it appears as though they should intersect for some micellar concentration between 50:30:0 mM and 33:20:0 mM. Presumably, this intersection between the two stability manifolds would be the location of a triple-point (or, more formally a bifurcation of co-dimension two), where for further increases in fluid inertia (or *Re*) there would be a transition directly from a steady symmetric to a time-dependent three-dimensional state, without first passing through a steady bifurcated state. This is also evident from the stability boundaries marked on Fig. 11(b). Future experiments with additional CPyCl:NaSal:NaCl fluids tuned to have properties intermediate to the 50:30:0 mM and 33:20:0 mM solutions could test this conjecture that we would find a direct transition from steady symmetric to time-dependent flow somewhere in this concentration regime.

V. CONCLUSIONS

We have explored the spatio-temporal dynamics of the response of a few well-characterized wormlike micellar solutions formulated from the CPyCl:NaSal:NaCl system to a well-defined extensional flow field generated within a microfluidic cross-slot device. Although the range of surfactant concentration only spans a factor of three, the fluids vary widely (by around three orders of magnitude) in terms of their linear and non-linear rheology. In the cross-slot device, at low strain rates ($Wi < 1$), the flow field for all the fluids is steady and symmetric and we observe a slender birefringent strand localized along the streamline flowing outwards from the stagnation point. In this regime we have shown how a combination of bulk pressure drop measurements and local birefringence measurements near the stagnation point can be used to provide a self-consistent measure of the apparent extensional viscosity of the fluid. At higher Weissenberg numbers most of the fluids (except for the most dilute and least elastic 33:20:0 mM fluid formulated without NaCl) exhibit a range of elastically-induced flow instabilities. The first of these transitions occurs at a low critical Weissenberg number (denoted $Wi_c^{(1)}$) and involves the development of a steady 2D flow asymmetry which is clearly manifested by the rotation and distortion of the birefringent strand originating from the stagnation point. At a second, much

higher critical Weissenberg number (denoted $Wi_c^{(2)}$) a 3D time-dependent flow instability develops.

Analysis of the critical shear rates and Weissenberg numbers of the instabilities and the detailed development of the bifurcation with Weissenberg number indicates that the critical conditions for the onset of these elastic instabilities are influenced both by inertial effects and by the form of the steady flow curve, in particular the extent of shear-thinning and the possibility of shear-banding. Our results indicate that, at least for this class of micellar fluid, it may be possible to closely predict the onset and nature of elastic instabilities in extensional flows from a detailed understanding of the steady shear rheology, provided it is measured over a sufficiently large range of shear rates. Moreover, we have also outlined a simple dimensionless measure of the relative importance of shear-thinning in a viscoelastic fluid, $S = \left(1 - d\ln\sigma / d\ln\dot{\gamma}\right)$, which can be readily evaluated from rheological measurements of any experimental test fluid or for any viscoelastic constitutive model being used in flow stability computations. This results in a more complete description of the competing roles of fluid viscoelasticity and the extent of shear-thinning in controlling the stability boundaries of complex viscoelastic flows. When combined with a suitable measure of fluid elasticity, such as the Weissenberg number (which captures the relevant magnitude of the elastic normal stresses in the fluid) and the Reynolds number (measuring the role of fluid inertia), complete flow stability diagrams can be constructed which demarcate different operating windows for steady symmetric, steady asymmetric and three-dimensional time-dependent flow. We have presented two different projections through this operating space in Figs. 11(b) and 12. A full three dimensional representation of the stability boundaries is provided by Fig. S1 in the Supplemental Material at [*URL to be inserted by publisher*]. It will be interesting to see if this new shear-thinning measure is useful in understanding trends observed in the critical conditions obtained from corresponding numerical simulations. Such simulations are just now becoming possible [32, 34, 35]. The ability to alter the critical conditions and nature of these viscoelastic flow instabilities by manipulating the fluid formulation (for example by simply adjusting the ionic environment to control the viscoelasticity, the degree of shear thinning and the extensibility of the micellar chains) may also

prove useful in industrial applications as well as for design of advanced control or mixing elements in lab-on-a-chip devices.

Acknowledgements

We gratefully acknowledge NASA Microgravity Fluid Sciences (Code UG) for support of this research under grant NNX09AV99G and thank Thomas Ober, Mónica Oliveira and Manuel Alves for helpful discussions. We would also like to thank Prof. Malcolm Mackley for invaluable insight and guidance in developing experimental diagnostics and flow geometries for probing the extensional rheology of complex fluids.

References

[1] R. G. Larson, *The Structure and Rheology of Complex Fluids* (Oxford University Press, New York, 1999).

[2] J.-F. Berret, in *Molecular Gels: Materials with Self-Assembled Fibrillar Networks*, edited by R. G. Weiss and P. Terech (Springer, Dordrecht, 2006).

[3] M. E. Cates and S. J. Candau, Journal of Physics: Condensed Matter **2**, 6869 (1990).

[4] H. Rehage and H. Hoffman, Molecular Physics **74**, 933 (1991).

[5] J. Appell, G. Porte, A. Khatory, F. Kern, and S. J. Candau, Journal de Physique II **2**, 1045 (1992).

[6] M. E. Cates and S. M. Fielding, Advances in Physics **55**, 799 (2006).

[7] J.-H. Mu, G.-Z. Li, X.-L. Jia, H.-X. Wang, and G.-Y. Zhang, Journal of Physical Chemistry B **106**, 11685 (2002).

[8] J.-H. Mu, G.-Z. Li, and H.-X. Wang, Rheologica Acta **41**, 493 (2002).

[9] S. Ezrahi, E. Tuval, and A. Aserin, Advances in Colloid and Interface Science **128-130**, 77 (2006).

[10] J. Yang, Current Opinion in Colloid & Interface Science **7**, 276 (2002).

[11] J. P. Rothstein, in *Rheology Reviews*, edited by D. M. Binding and K. Walters (The British Society of Rheology, Aberystwyth, 2008), Vol. 6, p. 1.

[12] J.-F. Berret, J. Appell, and G. Porte, Langmuir **9**, 2851 (1993).

[13] M. E. Helgeson, M. D. Reichert, Y. T. Hu, and N. J. Wagner, Soft Matter **5**, 3858 (2009).

[14] M. E. Helgeson, T. K. Hodgdon, E. W. Kaler, and N. J. Wagner, Journal of Colloid and Interface Science **349**, 1 (2010).

[15] P. Fischer, G. G. Fuller, and Z. Lin, Rheologica Acta **36**, 632 (1997).

[16] M. Chellamuthu and J. P. Rothstein, Journal of Rheology **52**, 865 (2008).

[17] B. Yesilata, C. Clasen, and G. H. McKinley, Journal of Non-Newtonian Fluid Mechanics **133**, 73 (2006).

[18] J. A. Pathak and S. D. Hudson, Macromolecules **39**, 8782 (2006).

[19] S. J. Haward, T. J. Ober, M. S. N. Oliveira, M. A. Alves, and G. H. McKinley, Soft Matter **8**, 536 (2012).

[20] A. F. Mendez-Sanchez, M. R. Lopez-Gonzalez, V. H. Rolon-Garrido, J. Perez-Gonzalez, and L. de Vargas, Rheologica Acta **42**, 56 (2003).

[21] M. Vasudevan, E. Buse, D. L. Lu, H. Krishna, R. Kalyanaraman, A. Q. Shen, B. Khomami, and R. Sureshkumar, Nature Materials **9**, 436 (2010).

[22] J. Soulages, M. S. N. Oliveira, P. C. Sousa, M. A. Alves, and G. H. McKinley, Journal of Non-Newtonian Fluid Mechanics **163**, 9 (2009).

[23] E. S. Boek, J. T. Padding, V. J. Anderson, P. M. J. Tardy, J. P. Crawshaw, and J. R. A. Pearson, Journal of Non-Newtonian Fluid Mechanics **126**, 39 (2005).

[24] P. E. Arratia, C. C. Thomas, J. Diorio, and J. P. Gollub, Physical Review Letters **96**, 144502 (2006).

[25] A. Groisman and V. Steinberg, Nature **410**, 905 (2001).

[26] A. Groisman, M. Enzelberger, and S. R. Quake, Science **300**, 955 (2003).

[27] T. T. Perkins, D. E. Smith, and S. Chu, Science **276**, 2016 (1997).

[28] D. E. Smith and S. Chu, Science **281**, 1335 (1998).

[29] P. A. Stone, S. D. Hudson, P. Dalhaimer, D. E. Discher, E. J. Amis, and K. B. Migler, Macromolecules **39**, 7144 (2006).

[30] S. J. Haward, V. Sharma, and J. A. Odell, Soft Matter **7**, 9908 (2011).
[31] R. J. Poole, M. A. Alves, and P. J. Oliveira, Physical Review Letters **99**, 164503 (2007).
[32] G. N. Rocha, R. J. Poole, M. A. Alves, and P. J. Oliveira, Journal of Non-Newtonian Fluid Mechanics **156**, 58 (2009).
[33] L. Xi and M. D. Graham, Journal of Fluid Mechanics **622**, 145 (2009).
[34] M. S. N. Oliveira, F. T. Pinho, R. J. Poole, P. J. Oliveira, and M. A. Alves, Journal of Non-Newtonian Fluid Mechanics **160**, 31 (2009).
[35] A. M. Afonso, M. A. Alves, and F. T. Pinho, Journal of Non-Newtonian Fluid Mechanics **165**, 743 (2010).
[36] J. A. Odell, in *Handbook of Experimental Fluid Mechanics*, edited by C. Tropea, Y. L. Yarin and J. F. Foss (Springer-Verlag, Heidelberg, 2007), p. 724.
[37] G. G. Fuller, *Optical Rheometry of Complex Fluids* (Oxford University Press, New York, 1995).
[38] H. Rehage and H. Hoffman, Journal of Physical Chemistry **92**, 4712 (1988).
[39] L. Abezgauz, K. Kuperkar, P. A. Hassan, O. Ramon, P. Bahadur, and D. Danino, **342**, 83 (2010).
[40] M. E. Cates, Journal of Physical Chemistry **94**, 371 (1990).
[41] N. A. Spenley, M. E. Cates, and T. C. McLeish, Physical Review Letters **71**, 939 (1993).
[42] M. S. Turner and M. E. Cates, Langmuir **7**, 1590 (1991).
[43] C. J. Pipe, T. S. Majmudar, and G. H. McKinley, Rheologica Acta **47**, 621 (2008).
[44] T. J. Ober, J. Soulages, and G. H. McKinley, Journal of Rheology **55**, 1127 (2011).
[45] R. W. Mair and P. T. Callaghan, Europhysics Letters **36**, 719 (1996).
[46] J. Y. Lee, G. G. Fuller, N. E. Hudson, and X.-F. Yuan, Journal of Rheology **49**, 537 (2005).
[47] S. Lerouge and J.-F. Berret, Advances in Polymer Science **230**, 1 (2009).
[48] P. T. Callaghan, M. E. Cates, C. J. Rofe, and J. B. A. F. Smeulders, Journal de Physique II **6**, 375 (1996).
[49] R. B. Bird, R. C. Armstrong, and O. Hassager, *Dynamics of Polymeric Liquids* (John Wiley and Sons, New York, 1987).
[50] V. M. Entov and E. J. Hinch, Journal of Non-Newtonian Fluid Mechanics **72**, 31 (1997).
[51] S. L. Anna and G. H. McKinley, Journal of Rheology **45**, 115 (2001).
[52] L. E. Rodd, T. P. Scott, J. J. Cooper-White, and G. H. McKinley, Applied Rheology **15** (2005).
[53] A. Bhardwaj, E. Miller, and J. P. Rothstein, Journal of Rheology **51**, 693 (2007).
[54] N. J. Kim, C. J. Pipe, K. H. Ahn, S. J. Lee, and G. H. McKinley, Korea-Australia Rheology Journal **22**, 31 (2010).
[55] P. G. De Gennes, Journal of Chemical Physics **60**, 5030 (1974).
[56] R. G. Larson and J. J. Magda, Macromolecules **22**, 3004 (1989).
[57] L. E. Rodd, T. P. Scott, D. V. Boger, J. J. Cooper-White, and G. H. McKinley, Journal of Non-Newtonian Fluid Mechanics **129**, 1 (2005).
[58] L. E. Rodd, J. J. Cooper-White, D. V. Boger, and G. H. McKinley, Journal of Non-Newtonian Fluid Mechanics **143**, 170 (2007).

[59] Z. Li, X.-F. Yuan, S. J. Haward, J. A. Odell, and S. Yeates, Rheologica Acta **50**, 277 (2011).
[60] Z. Li, X.-F. Yuan, S. J. Haward, J. A. Odell, and S. Yeates, Journal of Non-Newtonian Fluid Mechanics **166**, 951 (2011).
[61] L. Campo-Deaño, F. J. Galindo-Rosales, F. T. Pinho, M. A. Alves, and M. S. N. Oliveira, Journal of Non-Newtonian Fluid Mechanics **166**, 1286 (2011).
[62] C. D. Meinhart, S. T. Wereley, and M. H. B. Gray, Measurement Science and Technology **11**, 809 (2000).
[63] M. Shribak and R. Oldenbourg, Applied Optics **42**, 3009 (2003).
[64] R. G. Larson, Rheologica Acta **31**, 213 (1992).
[65] P. Pakdel and G. H. McKinley, Physics of Fluids **10**, 1058 (1998).
[66] S. Gulati, D. Liepmann, and S. J. Muller, Physical Review E **78**, 036314 (2008).
[67] S. Gulati, C. S. Dutcher, D. Liepmann, and S. J. Muller, Journal of Rheology **54**, 375 (2010).
[68] S. J. Muller, Korea-Australia Rheology Journal **20**, 117 (2008).
[69] M. A. Fardin, D. Lopez, J. Croso, G. Gregoire, O. Cardoso, G. H. McKinley, and S. Lerouge, Physical Review Letters **104**, 178303 (2010).
[70] M. A. Fardin, T. J. Ober, C. Gay, G. Gregoire, G. H. McKinley, and S. Lerouge, Soft Matter **8**, 910 (2012).
[71] M. A. Fardin, T. J. Ober, C. Gay, G. Gregoire, G. H. McKinley, and S. Lerouge, Europhysics Letters **96**, 44004 (2011).
[72] P. Pakdel and G. H. McKinley, Physical Review Letters **77**, 2459 (1996).
[73] W. P. Cox and E. H. Merz, Journal of Polymer Science **28**, 619 (1958).
[74] H. M. Laun, Journal of Rheology **30**, 459 (1986).
[75] V. Sharma and G. H. McKinley, Rheologica Acta **In Press** (2011).

Table 1: Fitting parameters for the Carreau-Yasuda and Maxwell models to the steady and oscillatory shear data at 22 ˚C.

FLUID	Carreau-Yasuda					Maxwell	
CPyCl:NaSal:NaCl [mM]	η_0 [Pa s]	η_∞ [Pa s]	$\dot{\gamma}^*$ [s^{-1}]	n [-]	a [-]	G_0 [Pa]	λ_M [s]
100:60:0	95.0	0.0089	0.14	0.01	3.0	30	3.10
66:40:0	10.5	0.0040	0.48	0.04	1.4	5.8	2.20
50:30:0	0.27	0.0025	11.1	0.24	1.0	2.8	0.12
33:20:0	0.10	0.0010	33.0	0.34	0.4	1.0	0.03
33:20:100	2.30	0.0030	1.00	0.17	2.0	2.6	0.90

Figure Captions

FIG. 1. (Color online) (a) Storage modulus (G', open symbols) and loss modulus (G'', closed symbols) as a function of frequency for the wormlike micellar test solutions under oscillatory shear in the AR-G2 cone-and-plate geometry. Data has been fitted with a single mode Maxwell model. (b) Normalized Cole-Cole plot derived from the data shown in (a).

FIG. 2. (Color online) (a) Stress and (b) viscosity as a function of shear rate for the wormlike micellar test solutions under steady shear in the AR-G2 cone-and-plate geometry (closed symbols) and the m-VROC microfluidic rheometer (open symbols). Data has been fitted with a Carreau-Yasuda generalized Newtonian fluid (GNF) model.

FIG. 3. (Color online) (a) Normalized mid-filament diameter as a function of time for wormlike micellar solutions in a capillary thinning extensional rheometer (CaBER). The initial gap was L_0 = 1 mm and the final gap L_f = 8 mm, providing corresponding aspect ratios of $\Lambda_0 = 0.167$ and $\Lambda_f = 1.33$, respectively with end-plates of diameter D_0 = 6 mm. The inset images show snapshots of the filaments seen in the 100:60:0 mM and 33:20:100 mM fluids at the moments indicated on the curves. (b) Trouton ratio, $Tr = \eta_E/\eta_0$, of the fluids determined from analysis of the data shown in (a).

FIG. 4. (Color online) (a) Optical micrograph of the 200 μm wide cross-slot geometry, showing the flow direction and the location of the stagnation point. (b) Schematic representation of the pressure drop measurements required to extract an apparent extensional viscosity in the cross-slot microchannel according to Eq. (11), where U is the superficial flow velocity in the channel.

FIG. 5. (Color online) Experimentally determined streamlines (left) and retardation (right) showing the development of asymmetric flow in the cross-slot geometry for a 100:60:0 mM CPyCl:NaSal:NaCl solution as the flow rate is increased: (a) steady symmetric flow at Q = 1.0 μL min^{-1}, (b) partially bifurcated flow at Q = 1.5 μL min^{-1} and (c) fully bifurcated flow at Q = 5.0 μL min^{-1}.

FIG. 6. (Color online) Examples of birefringence observed in a 100:60:0 mM CPyCl:NaSal:NaCl solution in the time-dependent flow regime at Q = 500 μL min^{-1}, Wi = 615, Re = 0.14. (a), (b), (c) and (d) were captured sequentially at time intervals of approximately 10 s. The colour scale represents retardation in the range 0-120 nm.

FIG. 7. (Color online) Birefringence observed with increasing flow rate for the various wormlike surfactant solutions indicated.

FIG. 8. (Color online) (a) Birefringence, Δn, measured at the stagnation point as a function of nominal imposed strain rate, $\dot{\varepsilon}$, for the various wormlike micellar test fluids in the steady symmetric flow regime. (b) Pressure drop measured in cross-slot flow (ΔP_{total}, solid symbols) and for flow around a corner of the cross (ΔP_{shear}, open symbols) as a function of the superficial flow velocity, $U = Q/2wd$, where the coloured arrows mark the onset of flow asymmetry. (c) Birefringence measured at the stagnation point as a function of the excess pressure drop, allowing the stress-optical coefficients of the fluids to be estimated from the gradient of straight-line fits through the origin. (d) Apparent extensional viscosity, $\eta_{E,app}$, as a function of the Weissenberg number, where dashed coloured lines mark the corresponding zero-shear viscosities. Inset shows the Trouton ratio, $Tr = \eta_{E,app}/\eta(\dot{\gamma})$.

FIG. 9. (Color online) Experimentally determined streamlines for (a) a 33:20:0 mM CPyCl:NaSal:NaCl solution flowing at Q = 4000 μL min^{-1}, Wi = 47.6, Re = 10.6; (b) a 50:30:0 mM CPyCl:NaSal:NaCl solution flowing at Q = 420 μL min^{-1}, Wi = 20, Re = 0.25. Measuring the location of the dividing streamline allows an asymmetry parameter, ΔQ, to be calculated according to Eq. 12. When the flow is symmetric, as in (a), ΔQ = 0; in the asymmetric example shown in (b), $\Delta Q \approx 0.25$. The velocity magnitude indicated by the colour scale is in units of m s^{-1}.

FIG. 10. (Color online) Asymmetry parameter, ΔQ, as a function of Weissenberg number for the various micellar test fluids in which the symmetry-breaking elastic instability was observed. For the 50:30:0 mM CPyCl:NaSal:NaCl test

fluid the bifurcation is well described by an equation of the form $\Delta Q \sim \left(Wi - Wi_c^{(1)}\right)^{0.5}$, where $Wi_c^{(1)} \approx$ 11.4, as shown by the dashed line.

FIG. 11. (Color online) (a) Shear stress as a function of shear rate for each of the wormlike micellar fluids, showing the critical shear rates on each flow curve that mark the onset of flow instabilities. For shear rates below the lower critical value, $\dot{\gamma}_c^{(1)}$ (solid symbols) the flow is steady and symmetric. Between the lower and upper critical shear rates the flow is steady but bifurcated. Above the upper critical shear rate, $\dot{\gamma}_c^{(2)}$ (open symbols) the flow becomes time-dependent. The transitions between flow regime correspond closely to changes in the local gradient of the flow curve. For clarity only the Carreau-Yasuda model fits to the experimental steady shear data presented in Fig. 2 are shown. (b) A state diagram showing the systematic variation with the degree of shear-thinning of the stability boundaries for onset of steady asymmetric flow in the cross-slot and for onset of time-dependent three-dimensional flows. The ordinate is a dimensionless measure of shear-thinning $\left[1-\eta_c/\eta(\dot{\gamma})\right]$ (see text for motivation), and the abscissa shows the dimensionless shear rate $\dot{\gamma}/\dot{\gamma}^*$ for each fluid scaled with the data provided in Table 1.

FIG. 12. (Color online) Stability diagram in Weissenberg-Reynolds number space showing the boundaries between elastic instabilities in the CPyCl:NaSal:NaCl test fluids. The solid symbols mark the lower critical Weissenberg number, $Wi_c^{(1)}$ for the onset of steady asymmetric flow, and the hollow symbols mark the upper critical Weissenberg number, $Wi_c^{(2)}$ for the onset of time-dependent flow.

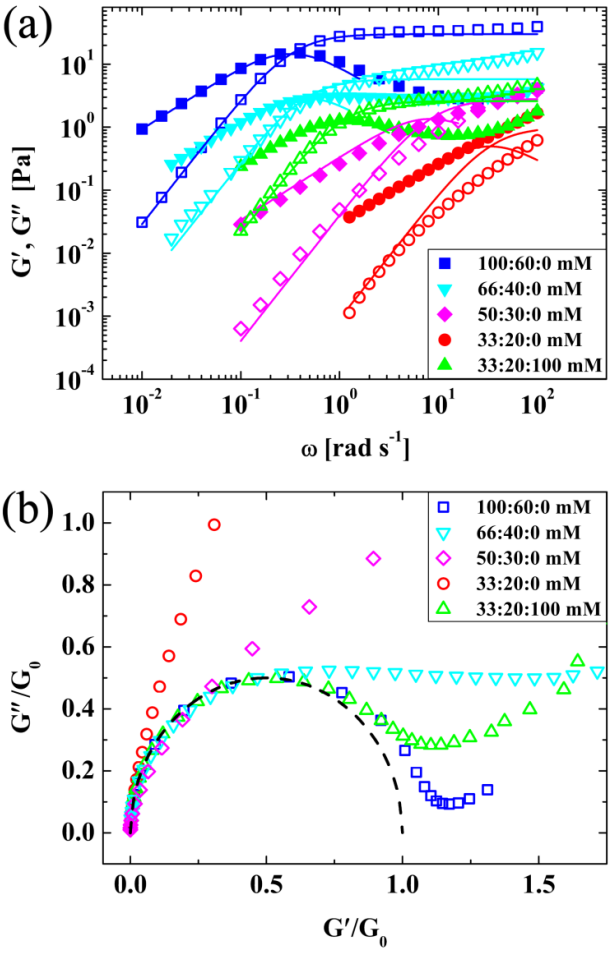

FIG. 1. (Color online) (a) Storage modulus (G', open symbols) and loss modulus (G'', closed symbols) as a function of frequency for the wormlike micellar test solutions under oscillatory shear in the AR-G2 cone-and-plate geometry. Data has been fitted with a single mode Maxwell model. (b) Normalized Cole-Cole plot derived from the data shown in (a).

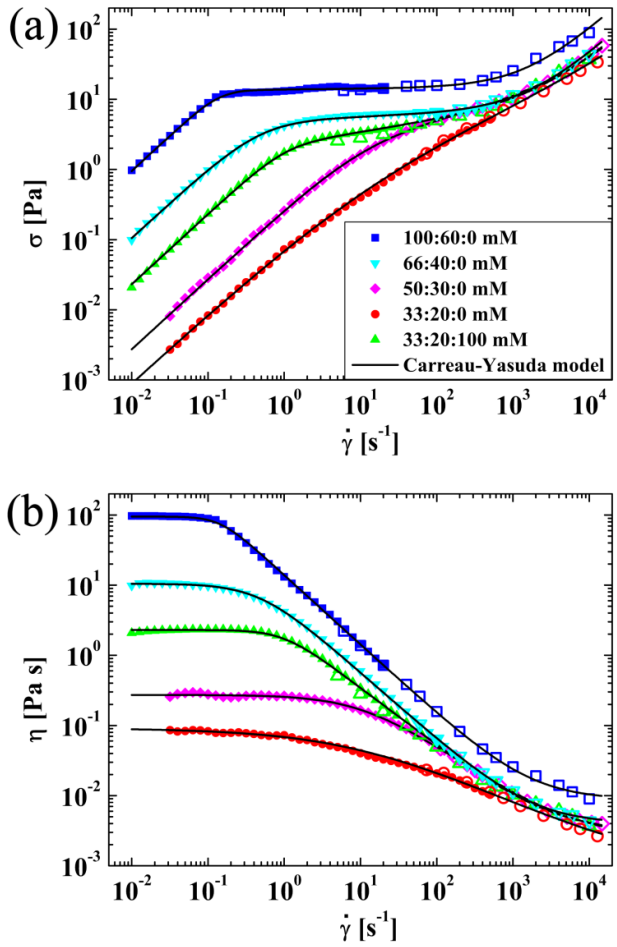

FIG. 2. (Color online) (a) Stress and (b) viscosity as a function of shear rate for the wormlike micellar test solutions under steady shear in the AR-G2 cone-and-plate geometry (closed symbols) and the m-VROC microfluidic rheometer (open symbols). Data has been fitted with a Carreau-Yasuda generalized Newtonian fluid (GNF) model.

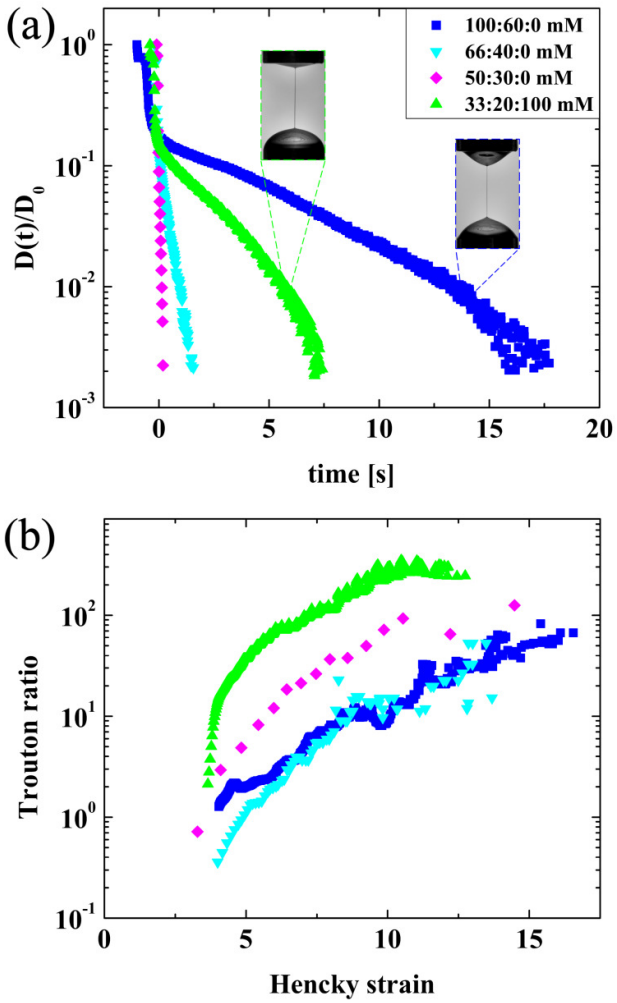

FIG. 3. (Color online) (a) Normalized mid-filament diameter as a function of time for wormlike micellar solutions in a capillary thinning extensional rheometer (CaBER). The initial gap was L_0 = 1 mm and the final gap L_f = 8 mm, providing corresponding aspect ratios of $\Lambda_0 = 0.167$ and $\Lambda_f = 1.33$, respectively with end-plates of diameter D_0 = 6 mm. The inset images show snapshots of the filaments seen in the 100:60:0 mM and 33:20:100 mM fluids at the moments indicated on the curves. (b) Trouton ratio, $Tr = \eta_E / \eta_0$, of the fluids determined from analysis of the data shown in (a).

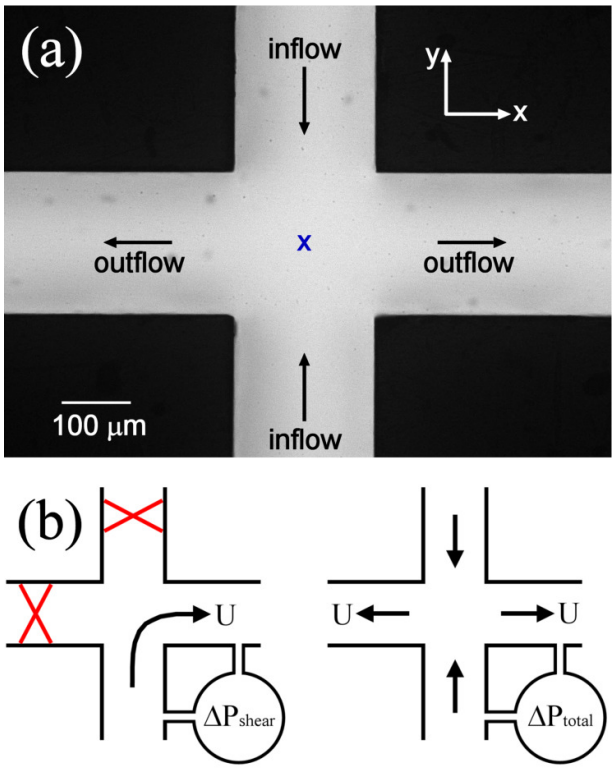

FIG. 4. (Color online) (a) Optical micrograph of the 200 μm wide cross-slot geometry, showing the flow direction and the location of the stagnation point. (b) Schematic representation of the pressure drop measurements required to extract an apparent extensional viscosity in the cross-slot microchannel according to Eq. 11, where *U* is the superficial flow velocity in the channel.

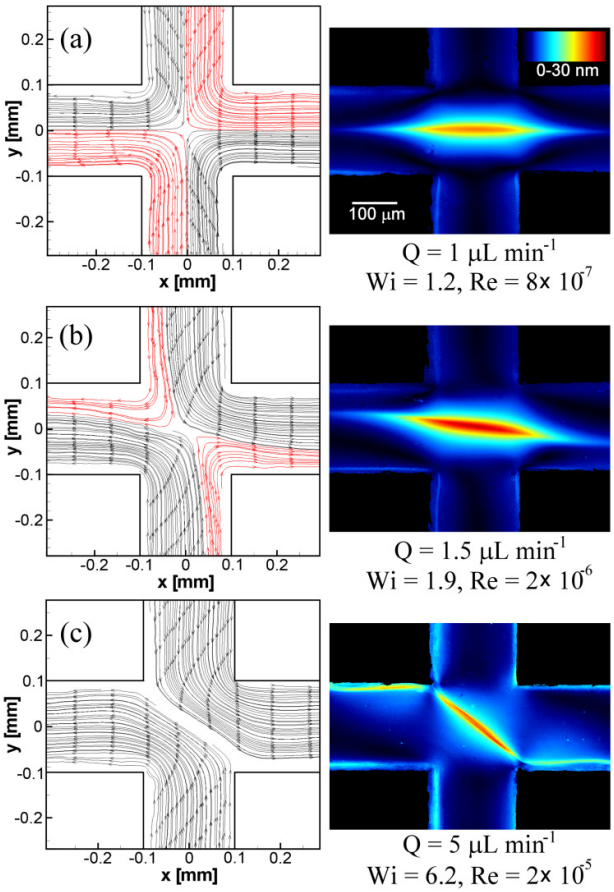

FIG. 5. (Color online) Experimentally determined streamlines (left) and retardation (right) showing the development of asymmetric flow in the cross-slot geometry for a 100:60:0 mM CPyCl:NaSal:NaCl solution as the flow rate is increased: (a) steady symmetric flow at Q = 1.0 μL min^{-1}, (b) partially bifurcated flow at Q = 1.5 μL min^{-1} and (c) fully bifurcated flow at Q = 5.0 μL min^{-1}.

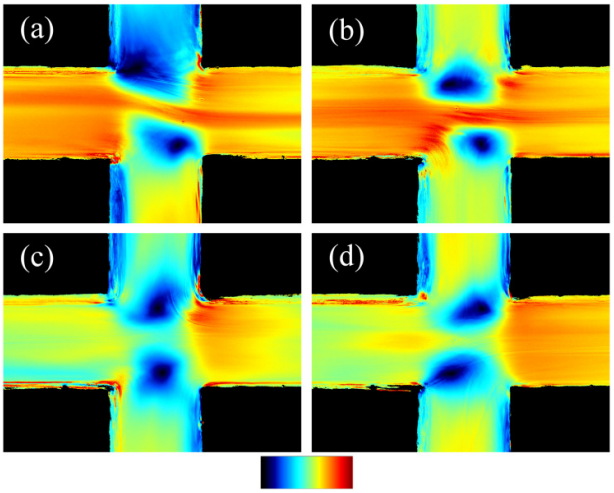

FIG. 6. (Color online) Examples of birefringence observed in a 100:60:0 mM CPyCl:NaSal:NaCl solution in the time-dependent flow regime at Q = 500 μL min^{-1}, Wi = 615, Re = 0.14. (a), (b), (c) and (d) were captured sequentially at time intervals of approximately 10 s. The colour scale represents retardation in the range 0-120 nm.

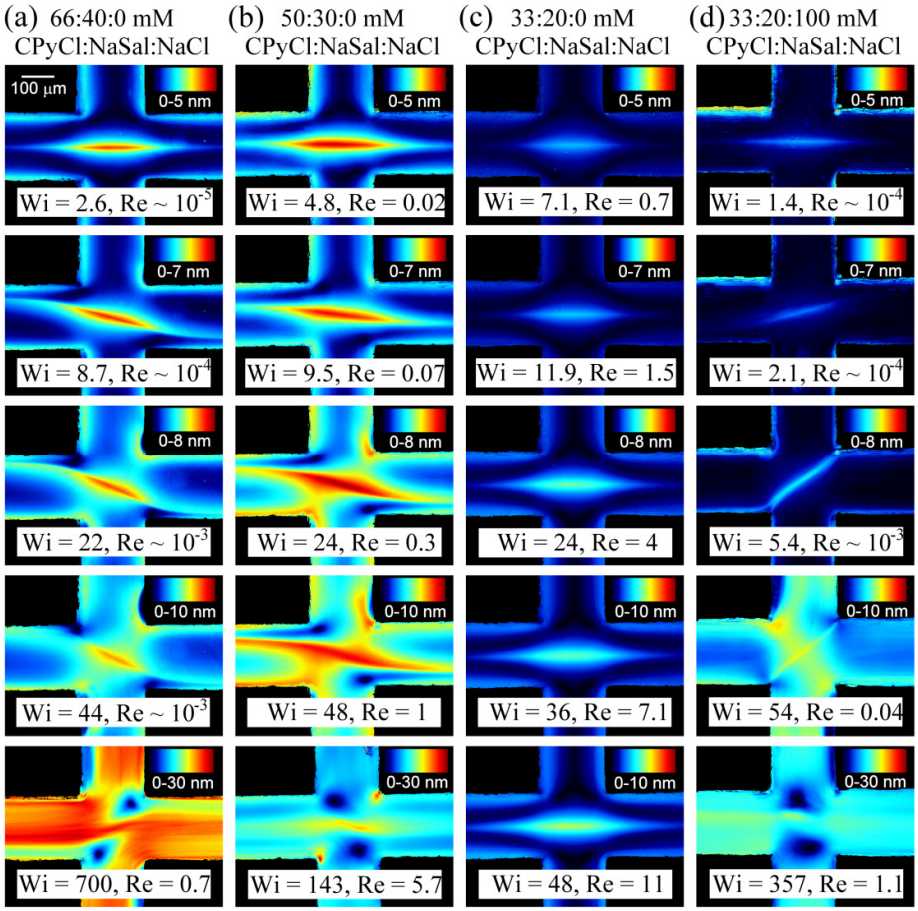

FIG. 7. (Color online) Birefringence observed with increasing flow rate for the various wormlike surfactant solutions indicated.

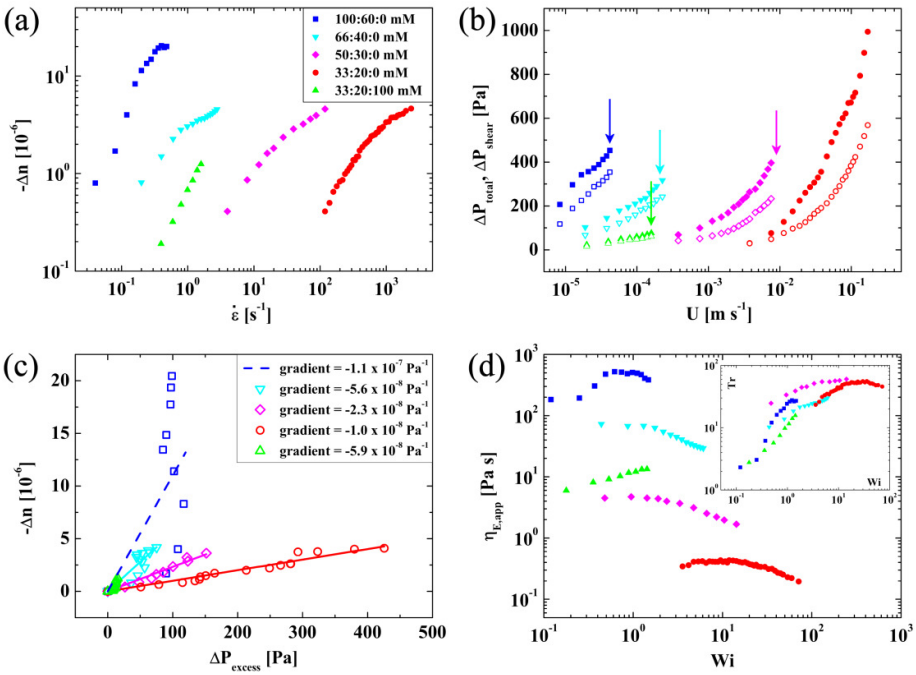

FIG. 8. (Color online) (a) Birefringence, Δn, measured at the stagnation point as a function of nominal imposed strain rate, $\dot{\varepsilon}$, for the various wormlike micellar test fluids in the steady symmetric flow regime. (b) Pressure drop measured in cross-slot flow (ΔP_{total}, solid symbols) and for flow around a corner of the cross (ΔP_{shear}, open symbols) as a function of the superficial flow velocity, $U = Q/2wd$, where the coloured arrows mark the onset of flow asymmetry. (c) Birefringence measured at the stagnation point as a function of the excess pressure drop, allowing the stress-optical coefficients of the fluids to be estimated from the gradient of straight-line fits through the origin. (d) Apparent extensional viscosity, $\eta_{E,app}$, as a function of the Weissenberg number, where dashed coloured lines mark the corresponding zero-shear viscosities. Inset shows the Trouton ratio, $Tr = \eta_{E,app}/\eta(\dot{\gamma})$.

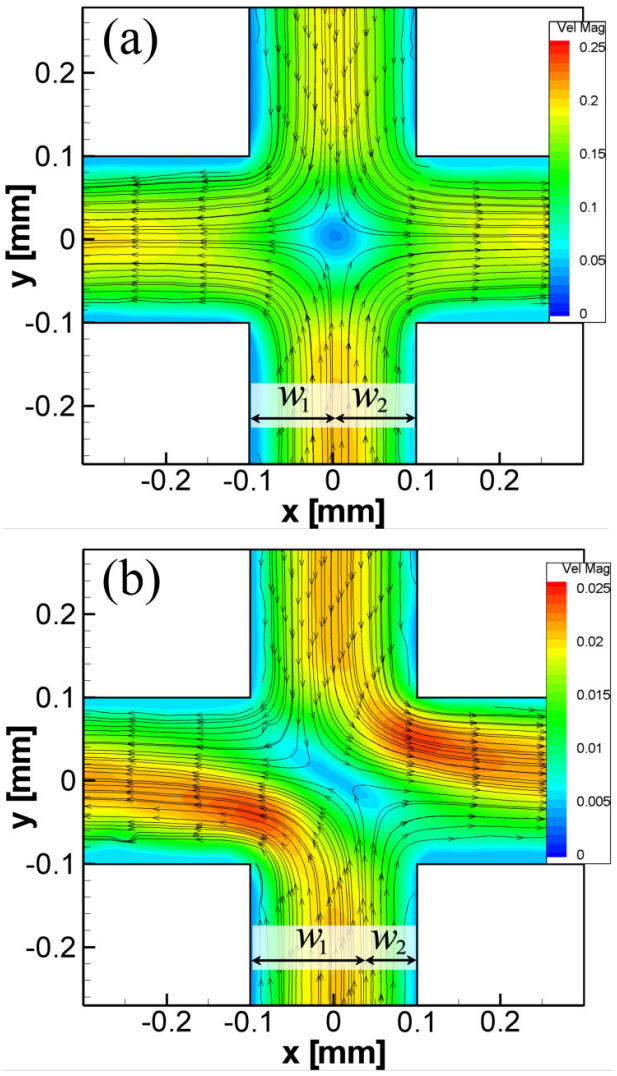

FIG. 9. (Color online) Experimentally determined streamlines for (a) a 33:20:0 mM CPyCl:NaSal:NaCl solution flowing at Q = 4000 μL min^{-1}, Wi = 47.6, Re = 10.6; (b) a 50:30:0 mM CPyCl:NaSal:NaCl solution flowing at Q = 420 μL min^{-1}, Wi = 20, Re = 0.25. Measuring the location of the dividing streamline allows an asymmetry parameter, ΔQ, to be calculated according to Eq. 12. When the flow is symmetric, as in (a), ΔQ = 0; in the asymmetric example shown in (b), $\Delta Q \approx 0.25$. The velocity magnitude indicated by the colour scale is in units of m s^{-1}.

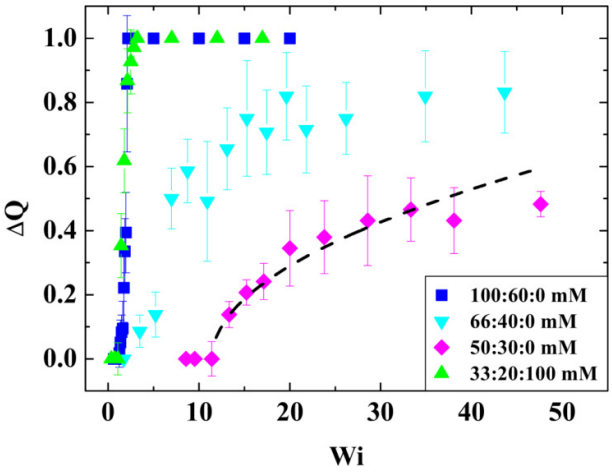

FIG. 10. (Color online) Asymmetry parameter, ΔQ, as a function of Weissenberg number for the various micellar test fluids in which the symmetry-breaking elastic instability was observed. For the 50:30:0 mM CPyCl:NaSal:NaCl test fluid the bifurcation is well described by an equation of the form $\Delta Q \sim \left(Wi - Wi_c^{(1)}\right)^{0.5}$, where $Wi_c^{(1)} \approx 11.4$, as shown by the dashed line.

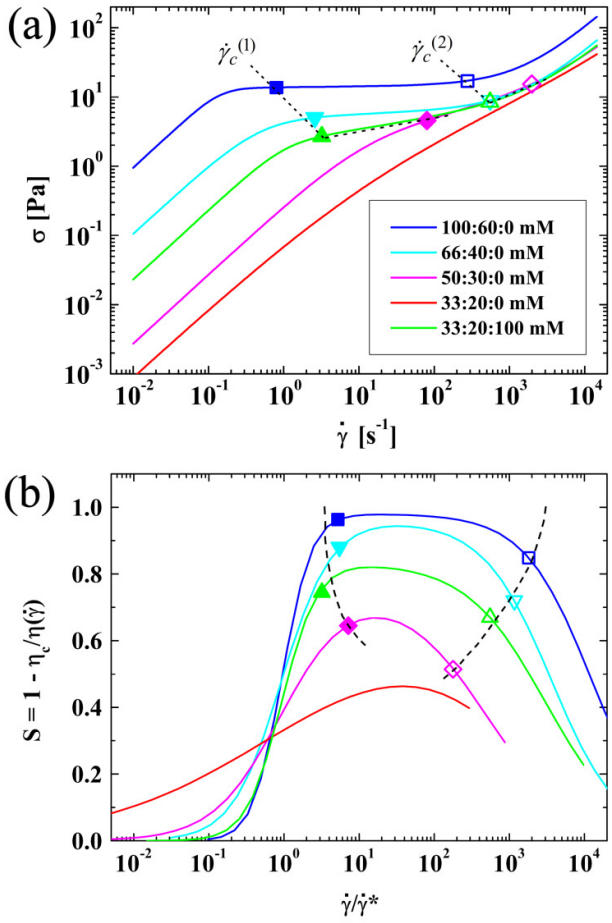

FIG. 11. (Color online) (a) Shear stress as a function of shear rate for each of the wormlike micellar fluids, showing the critical shear rates on each flow curve that mark the onset of flow instabilities. For shear rates below the lower critical value, $\dot{\gamma}_c^{(1)}$ (solid symbols) the flow is steady and symmetric. Between the lower and upper critical shear rates the flow is steady but bifurcated. Above the upper critical shear rate, $\dot{\gamma}_c^{(2)}$ (open symbols) the flow becomes time-dependent. The transitions between flow regime correspond closely to changes in the local gradient of the flow curve. For clarity only the Carreau-Yasuda model fits to the experimental steady shear data presented in Fig. 2 are shown. (b) A state diagram showing the systematic variation with the degree of shear-thinning of the stability boundaries for onset of steady asymmetric flow in the cross-slot and for onset of time-dependent three-dimensional flows. The ordinate is a dimensionless measure of shear-thinning $\left[1-\eta_c/\eta(\dot{\gamma})\right]$ (see text for motivation), and the abscissa shows the dimensionless shear rate $\dot{\gamma}/\dot{\gamma}^*$ for each fluid scaled with the data provided in Table 1.

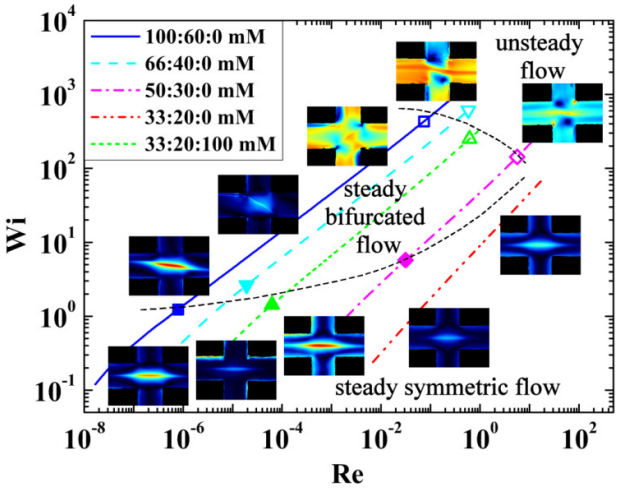

FIG. 12. (Color online) Stability diagram in Weissenberg-Reynolds number space showing the boundaries between elastic instabilities in the CPyCl:NaSal:NaCl test fluids. The solid symbols mark the lower critical Weissenberg number, $Wi_c^{(1)}$ for the onset of steady asymmetric flow, and the hollow symbols mark the upper critical Weissenberg number, $Wi_c^{(2)}$ for the onset of time-dependent flow.